Journal of Solid State Chemistry 181 (2008) 2530–2541

Contents lists available at ScienceDirect

Journal of Solid State Chemistry

journal homepage: www.elsevier.com/locate/jssc

Structure and magnetic properties of $Ca_2Fe_{1-x}Mn_xAlO_{5+\delta}$

M.D. Carvalho [a,*], L.P. Ferreira [b,c], J.C. Waerenborgh [d], E. Tsipis [d], A.B. Lopes [e], M. Godinho [f]

[a] CCMM/Dep. Química e Bioquímica, Faculdade de Ciências, Universidade de Lisboa, 1749-016 Lisboa, Portugal
[b] CFMC-UL, Faculdade de Ciências, Universidade de Lisboa, 1749-016 Lisboa, Portugal
[c] Dep. Física, Faculdade de Ciências e Tecnologia, Universidade de Coimbra, 3004-516 Coimbra, Portugal
[d] Dep. Química, ITN/CFMC-UL, Estrada Nacional 10, P-2686-953 Sacavém, Portugal
[e] Dep. de Engenharia Cerâmica e do Vidro, CICECO, Universidade de Aveiro, 3810-193 Aveiro, Portugal
[f] CFMC-UL/Dep. Física, Faculdade de Ciências, Universidade de Lisboa, 1749-016 Lisboa, Portugal

ARTICLE INFO

Article history:
Received 28 April 2008
Received in revised form
2 June 2008
Accepted 5 June 2008
Available online 10 June 2008

Keywords:
Brownmillerite structure
Oxygen stoichiometry
Mössbauer spectroscopy
Magnetic measurements

ABSTRACT

$Ca_2Fe_{1-x}Mn_xAlO_5$ ($0 \leqslant x \leqslant 1$) compounds were prepared by a self-combustion method under air ($x = 0$, 0.1, 0.2 and 0.3) and nitrogen ($x = 0.5$, 0.7 and 1.0). The samples prepared under nitrogen were successfully oxidized after short annealing under air. Both X-ray powder diffraction (XRD) Rietveld analysis and electron diffraction revealed that all compounds adopt the brownmillerite-type structure. All samples present an overall antiferromagnetic behaviour and data from magnetic measurements and Mössbauer spectroscopy allowed to conclude that the transition temperature decreases as Mn content increases for $x \leqslant 0.3$ and increases in the case of the $x \geqslant 0.5$ compounds. Except for $x = 1$, chemical disorder due to the occupancy of both octahedral and tetrahedral sites by different metals as well as the competition between different moments' orientation induce a complex magnetic behaviour characterized by magnetic frustration and canted antiferromagnetism. Mössbauer spectroscopy and chemical titrations also allowed to conclude about the preferential oxidation of Mn^{3+} over Fe^{3+}, obtained by thermal treatment under air of the $x = 0.5$ and 0.7 compositions.

1. Introduction

The brownmillerite-type structure ($A_2BB'O_5$) can be described as an oxygen-deficient perovskite, resulting in a sequence of regular alternating layers of corner-sharing BO_6 octahedra (O) and $B'O_4$ tetrahedra (T) (Fig. 1). Depending on the synthesis route and B cations, these compounds crystallize in one of the following space group symmetries: *Ibm*2, *Icmm* or *Pcmn*, where *Ibm*2 and *Pcmn* describe fully ordered structures in terms of cation and oxygen displacements in the tetrahedral chains [1,2]. Structural stabilization can be achieved when B' sites are occupied by cations with preference for tetrahedral coordination, such as Ga and Al [3].

Brownmillerite compounds containing manganese have been studied recently due to their potential application as low-field colossal magnetoresistance materials, like naturally layered manganates. Several studies on $A_2MnBO_{5+\delta}$ (A = Ca, Sr; B = Al, Ga) compounds showed the ability of the structure to accommodate oxygen, and compositions like $Ca_2MnAlO_{5.5}$ [4] and $Sr_2MnGaO_{5.5}$ [5] were obtained by oxidizing treatments of the as-prepared compounds A_2MnBO_5. In the case of the $Ca_2MnBO_{5.5}$ compound, it represents the $n = 3$ brownmillerite structure where the OTOTOT layer sequence for $\delta \approx 0$ is replaced by the OOOTOOOT sequence for $\delta \approx 0.5$ [5]. A different sequence characterizes the $Ca_{2.5}Sr_{0.5}GaMn_2O_8$ compound ($n = 2$ brownmillerite structure—OOTOOT), also presenting a mixed valence for manganese ions [6]. Regarding the $n = 1$ brownmillerite compounds ($A_2BB'O_5$), some oxygen overstoichiometry is also possible, these compositions being best represented by $A_2BB'O_{5+\delta}$. Depending on the synthesis conditions, δ assumes small values, varying from −0.03 to 0.1 for $Sr_2MnGaO_{5+\delta}$ [7,8], 0.09 for $Ca_2MnGaO_{5+\delta}$ [3] and 0.035 for $SrCaMnGaO_{5+\delta}$ [9].

Both Ca_2FeAlO_5 [10,11] and Ca_2MnAlO_5 [12] phases have the *Ibm*2 brownmillerite structure and are antiferromagnetic below 340 K [11] and 152 K, respectively. In Ca_2FeAlO_5, the Fe moments seem to be aligned in the a–c plane [13] while in Ca_2MnAlO_5 the Mn moments are oriented along the b direction [12]. None of these compounds present oxygen overstoichiometry ($\delta = 0$), although Ca_2FeAlO_5 was prepared under air and the manganese brownmillerite under nitrogen flow.

Solid solutions between Ca_2AlFeO_5 and Ca_2AlMnO_5 were prepared using the ceramic method, according to Zotzl and

* Corresponding author. Fax: +351 217500088.
E-mail address: mdcarvalho@fc.ul.pt (M.D. Carvalho).

0022-4596/$ - see front matter © 2008 Elsevier Inc. All rights reserved.
doi:10.1016/j.jssc.2008.06.008

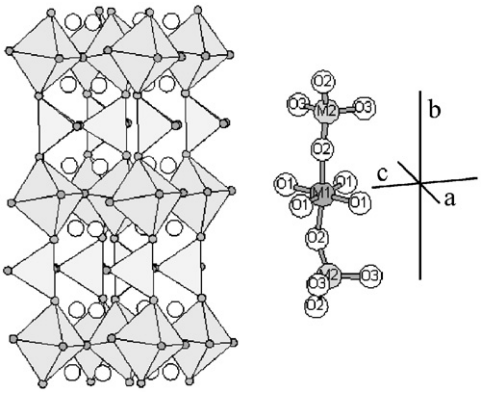

Fig. 1. Schematic representations of the brownmillerite structure, the right one showing two tetrahedra and one octahedron.

Pollmann [14] and references therein. However, only the cell parameters of a few compositions were reported and, also due to the synthesis conditions used, a deeper structure determination is required.

In this work, the synthesis, structural characterization and magnetic properties of the $Ca_2Fe_{1-x}Mn_xAlO_{5+\delta}$ compounds ($0 \leqslant x \leqslant 1$) obtained under different atmospheres are reported. X-ray powder diffraction (XRD), transmission electron microscopy (TEM), Mohr salt titrations, Mössbauer spectroscopy and magnetic measurements were used to investigate the compounds.

2. Experimental

Ceramic powders of $Ca_2Fe_{1-x}Mn_xAlO_{5+\delta}$ ($0 \leqslant x \leqslant 1.0$) were prepared by a self-combustion route. The starting materials of reagent grade ($CaCO_3$, $MnCO_3$, $FeC_2O_4 \cdot 2H_2O$ and $Al(OH)_3$) were mixed in the appropriate molar ratios and dissolved in nitric acid. An equivalent molar quantity of urea (relatively to the metals) was added to the obtained solutions and heated up to the auto-ignition. The resulting powders were heated at 1173 K. For the samples with $0 \leqslant x \leqslant 0.3$, further calcinations were performed in air at 1553 K, as previously reported for the $x = 0$ phase [11]. Attempts to prepare the compounds with $x > 0.3$ in air always resulted in a mixture of phases. Single phases with $x = 0.5$, 0.7 and 1.0 were prepared by the same method using a nitrogen flow on the thermal treatments at 1523 K. Additional thermal treatments at 873 K for 6 h under air were carried out to investigate the stability of the samples.

XRD was performed using a Philips PW 1730 powder diffractometer, operating with a Cu-$K\alpha$ radiation and previously calibrated using a Si standard. Structural Rietveld refinements of the XRD patterns collected between 15° and 120° (2θ), in steps of 0.02°, were performed with the FullProf software [15]. A sixth-order polynomial function was used to model the background level. The peak shapes were fitted to a pseudo-Voigt function and two asymmetry parameters were used. A preferred orientation correction was included and the total occupation factors were fixed taking into account the sample stoichiometry and assuming fully occupied oxygen sites. Individual thermal parameters were refined constraining their values to be identical for symmetrically equivalent sites.

Electron diffraction (ED) patterns of the as-prepared samples $Ca_2Fe_{1-x}Mn_xAlO_{5+\delta}$ for $x = 0.2$, 0.5 and 1.0 were obtained using a 300 kV Hitachi H9000 TEM. The samples were crushed and the powder was dispersed in ethanol and deposited on a TEM grid.

Mohr salt titrations were carried out to determine the mean oxidation state of the transition metal ions. The total M^{4+} amount (M = Fe and Mn) and oxygen content present in the samples were calculated.

The Mössbauer spectra were collected at 363 K, room temperature and 4 K in transmission mode using a conventional constant-acceleration spectrometer and a 25 mCi ^{57}Co source in a Rh matrix. The low-temperature measurements were performed using a bath cryostat with the sample immersed in liquid He. Above room temperature the spectra were obtained using a Wissel MBF-1100 furnace. The velocity scale was calibrated using an α-Fe foil. The spectra were fitted to Lorentzian lines using a non-linear least-squares method [16] and to distributions of quadrupole or magnetic splittings according to the histogram method.

Magnetization measurements were performed using a SQUID magnetometer (Quantum Design MPMS) as a function of temperature, $M(T)$, and applied magnetic field, $M(H)$. The $M(T)$ curves were obtained at 0.5, 5 and 50 mT for temperatures ranging from 2 to 360 K. Data were collected in increasing temperature after both zero-field cooling (ZFC) and field cooling (FC) procedures. The isothermal $M(H)$ curves were measured for

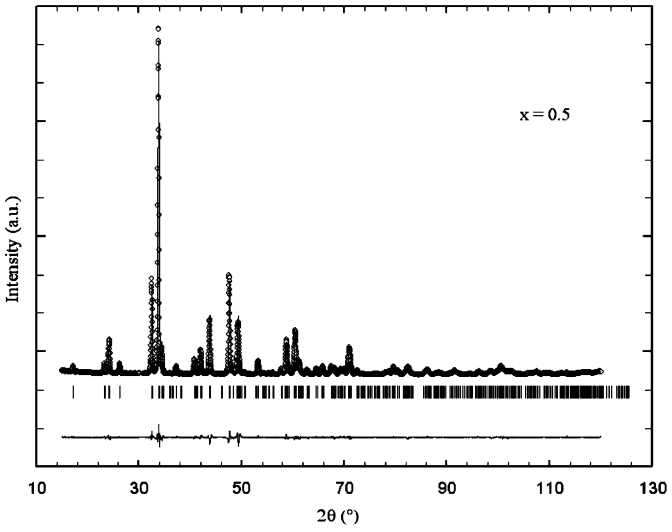

Fig. 2. Observed (points) and calculated (solid line) Rietveld refinement plots of the XRD patterns for the $x = 0.5$ compound prepared under nitrogen. The difference between observed and calculated is shown at the bottom of each pattern. Tick marks represent allowed reflections.

Table 1
Cell parameters values and conventional Rietveld factors from the XRD data of the as-prepared compounds $Ca_2Fe_{1-x}Mn_xAlO_5$

Sample	a (Å)	b (Å)	c (Å)	Vol. (Å^3)	CR_{wp}	CR_p	R_{Bragg}	M^{4+} (f.u.)
$x = 0$	5.5639(1)	14.5131(2)	5.3457(1)	431.66(2)	8.97	7.30	2.65	0
$x = 0.1$	5.5481(2)	14.5740(5)	5.3363(2)	431.48(2)	10.7	8.66	2.58	0.04
$x = 0.2$	5.5373(2)	14.6096(5)	5.3256(2)	430.84(2)	9.82	7.97	2.38	0.04
$x = 0.3$	5.5274(2)	14.6515(5)	5.3180(2)	430.68(2)	10.6	8.38	2.90	0.05
$x = 0.5$	5.5106(2)	14.7579(6)	5.2933(2)	430.48(3)	10.3	8.23	2.68	0
$x = 0.7$	5.4965(1)	14.8425(3)	5.2744(1)	430.29(2)	11.3	8.92	3.18	0
$x = 1$	5.4687(1)	15.0026(3)	5.2425(1)	430.12(2)	12.5	8.84	4.32	0

The M^{4+} values per formula unit correspond to the iodometric titration results.

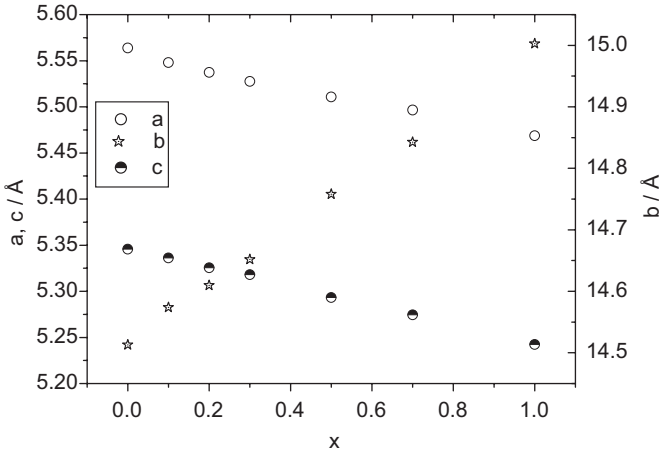

Fig. 3. Cell parameters variation of the as-prepared compounds $Ca_2Fe_{1-x}Mn_xAlO_5$.

magnetic fields up to 5.5 T. Isothermal remanent magnetization (IRM) and thermoremanent magnetization (TRM) measurements were carried out in zero magnetic field, after cooling the samples from room temperature to 5 K under zero applied field (IRM) or under 0.5 T (TRM), setting the field to the measuring value (up to 5.5 T) for 60 s and then reducing it to zero.

3. Results and discussion

3.1. Structural characterization

3.1.1. As-prepared compounds

All the compounds (prepared under air or nitrogen) were successfully synthesized and the XRD patterns were consistent with the brownmillerite structure. The lattice parameters and unit cell volume were obtained from the Rietveld refinements. For Ca_2FeAlO_5, the *Ibm*2 space group was adopted, and Al^{3+} ions were considered to occupy both tetrahedral and octahedral sites (3/4 and 1/4, respectively), as previously reported [10,11].

Table 2
Refined atomic positions for the $Ca_2Fe_{1-x}Mn_xAlO_5$ (as-prepared samples), obtained from Rietveld analysis of the XRD data (S.G—*Ibm*2)

	Ca (8*c*)	*M* (4*a*)	*M* (4*b*)	O1 (8*c*)	O2 (8*c*)	O3 (4*b*)
$x = 0$						
x	0.0267(2)	0	0.9287(3)	0.2551(6)	0.0675(4)	0.8605(7)
y	0.10839(5)	0	0.25	0.9882(1)	0.1444(2)	0.25
z	0.4913(5)	0	0.9541(4)	0.247(2)	0.0220(7)	0.6177(8)
B (Å^2)	0.57(2)	0.48(2)	0.38(4)	0.75(4)	0.75(4)	0.8(1)
Occup	1	0.375(Fe); 0.125(Al)	0.125(Fe); 0.375(Al)	1	1	0.5
$x = 0.1$						
x	0.0262(2)	0	0.9301(4)	0.2532(9)	0.0648(5)	0.863(1)
y	0.10883(8)	0	0.25	0.9880(2)	0.1447(2)	0.25
z	0.4946(6)	0	0.9564(6)	0.2459(2)	0.027(1)	0.620(1)
B (Å^2)	0.69(3)	0.59(3)	0.24(5)	0.95(6)	0.95(6)	1.3(2)
Occup	1	0.34(Fe); 0.11(Al); 0.05(Mn)	0.11(Fe); 0.39(Al)	1	1	0.5
$x = 0.2$						
x	0.0264(2)	0	0.9316(4)	0.2534(9)	0.0648(4)	0.8647(9)
y	0.10932(8)	0	0.25	0.9880(2)	0.1450(2)	0.25
z	0.4949(7)	0	0.9573(6)	0.245(2)	0.027(1)	0.620(1)
B (Å^2)	0.71(3)	0.52(3)	0.87(5)	0.91(5)	0.91(5)	1.2(2)
Occup	1	0.27(Fe); 0.13(Al); 0.1(Mn)	0.13(Fe); 0.37(Al)	1	1	0.5
$x = 0.3$						
x	0.0262(2)	0	0.9326(4)	0.2537(9)	0.0641(5)	0.867(1)
y	0.10988(8)	0	0.25	0.9884(2)	0.1458(2)	0.25
z	0.4939(7)	0	0.9577(6)	0.244(2)	0.028(1)	0.624(1)
B (Å^2)	0.80(3)	0.34(4)	1.08(6)	0.83(6)	0.83(6)	1.3(2)
Occup	1	0.20(Fe); 0.15(Al); 0.15(Mn)	0.15(Fe); 0.35(Al)	1	1	0.5
$x = 0.5$						
x	0.0257(2)	0	0.9305(4)	0.2553(9)	0.0644(5)	0.866(1)
y	0.11045(7)	0	0.25	0.9891(2)	0.1464(2)	0.25
z	0.4931(6)	0	0.9538(6)	0.242(2)	0.028(1)	0.622(1)
B (Å^2)	0.64(3)	0.38(3)	0.57(6)	1.14(6)	1.14(6)	1.1(2)
Occup	1	0.15(Fe); 0.10(Al); 0.25(Mn)	0.10(Fe); 0.40(Al)	1	1	0.5
$x = 0.7$						
x	0.0261(2)	0	0.9300(4)	0.253(1)	0.0648(5)	0.862(1)
y	0.11079(7)	0	0.25	0.9884(2)	0.1468(2)	0.25
z	0.4927(6)	0	0.9541(6)	0.249(2)	0.0350(9)	0.625(1)
B (Å^2)	0.72(3)	0.51(3)	0.52(5)	0.99(6)	0.99(6)	1.4(2)
Occup	1	0.09(Fe); 0.06(Al); 0.35(Mn)	0.06(Fe); 0.44(Al)	1	1	0.5
$x = 1.0$						
x	0.0266(2)	0	0.9317(5)	0.254(1)	0.0662(6)	0.857(1)
y	0.11153(7)	0	0.25	0.9870(2)	0.1474(2)	0.25
z	0.4976(7)	0	0.9577(6)	0.247(2)	0.036(1)	0.621(2)
B (Å^2)	0.84(3)	0.54(3)	0.19(6)	0.85(6)	0.85(6)	1.2(2)
Occup	1	0.5(Mn)	0.5(Al)	1	1	0.5

The same space group was assumed for all samples since Ca_2MnAlO_5 also adopts the *Ibm*2 symmetry [12]. The manganese ions were considered to only occupy octahedral sites, as neutron powder diffraction on Ca_2MnAlO_5 compound [12] showed no evidence for Mn–Al mixed occupancy. For the $0<x<1$ samples, different occupation site ratios for iron and aluminium were attempted, including the one based on our Mössbauer results for iron ions occupation, as described in Section 3.2. This latter structural model led to the best refinement profile. The total occupation factors were fixed taking into account sample stoichiometry and assuming fully occupied oxygen sites. Fig. 2 exemplifies the Rietveld refinement plot of the XRD patterns for the $x = 0.5$ compound (prepared under nitrogen).

Table 1 summarizes the cell parameters and the conventional reliability factors of the Rietveld refinements for each compound, as well as the amounts of M^{4+} ions determined by titration. A systematic decrease of the *a* and *c* cell parameters and the increase of *b* was observed with the increase of manganese content (Fig. 3). As both Mn^{3+} and Fe^{3+} ions with octahedral coordination have the same ionic radius ($r_{(VI)} = 0.645$ Å) [17], it is clear that the cell parameters variation between $x = 0$ and 1.0 compounds was controlled by the Jahn–Teller effect of the Mn^{3+} ions. This effect will be further discussed. The results obtained for the $x = 0$ and 1.0 compositions are in good agreement with previous studies [10–12]. Table 2 gives the atomic positions obtained from the refinements and a schematic representation of the structure is shown in Fig. 1. Some selected bond lengths and angles, as well as the calculated strain parameter defined as $\sigma_{JT} = \sqrt{1/6\sum[(B\text{–O})_i - \langle B\text{–O}\rangle]^2}$ [9], are presented in Table 3 (in the case of $x = 0$, this parameter is included for comparison). For all the obtained compounds, as usually observed in the brownmillerite structure, the MnO_6 octahedron is characterized by four short equatorial M–O1 distances and two long apical M–O2 ones oriented along the *b*-axis, while oxygen tetrahedra are slightly compressed along this axis. Axial distortions of the BO_6 octahedra of the brownmillerite structure $A_2BB'O_5$ are observed not only for cations exhibiting the Jahn–Teller effect, but also for cations

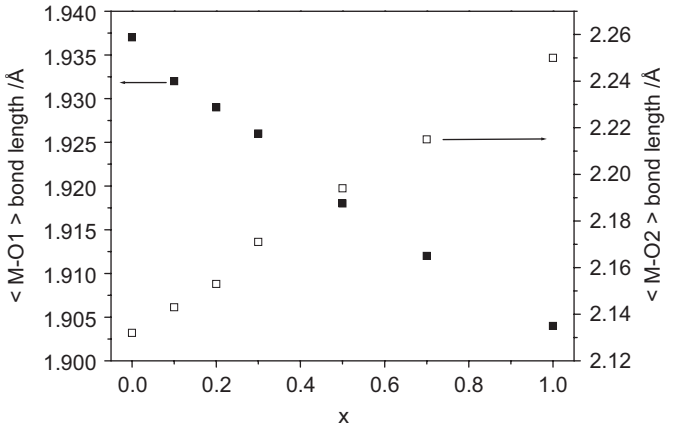

Fig. 4. Mean bond length of the *M*–O distances for the as-prepared compounds $Ca_2Fe_{1-x}Mn_xAlO_5$.

Table 3
Selected bond lengths (Å) and bond angles (deg) for the as-prepared $Ca_2Fe_{1-x}Mn_xAlO_5$ compounds (strain parameter: $\sigma_{JT} = \sqrt{1/6\sum[(B\text{–O})_i\text{-}\langle B\text{–O}\rangle]^2}$)

X	M_{oct}–O		M_{tetra}–O		σ_{JT}	M_{tet}–O2–M_{oct}	O1–M_{oct}–O1	O2–M_{oct}–O2
0	M–O1	1.946(6) (2*x*)	M–O2	1.755(2) (*x*2)	0.092[a]	140.3(1)	94.6(3)	173.7(2)
	M–O1	1.928(6) (2*x*)	M–O3	1.838(5)			87.3(5)	
	M–O2	2.132(2) (2*x*)	M–O3	1.832(4)			90.8(3)	
	$\langle M_{oct}\text{–}O\rangle$	*2.002*	$\langle M_{tet}\text{–}O\rangle$	*1.795*			178.1(6)	
0.1	*M*–O1	1.928(8) (2*x*)	*M*–O2	1.750(4) (*x*2)	0.099	140.9(1)	94.3(5)	172.2(3)
	M–O1	1.937(9) (2*x*)	*M*–O3	1.833(7)			87.3(7)	
	M–O2	2.143(3) (2*x*)	*M*–O3	1.844(6)			91.1(5)	
	$\langle M_{oct}\text{–}O\rangle$	*2.003*	$\langle M_{tet}\text{–}O\rangle$	*1.794*			178.4(8)	
0.2	*M*–O1	1.919(8) (2*x*)	*M*–O2	1.742(3) (*x*2)	0.106	141.5(1)	94.6(5)	172.2(3)
	M–O1	1.939(8) (2*x*)	*M*–O3	1.838(6)			87.3(7)	
	M–O2	2.153(3) (2*x*)	*M*–O3	1.850(6)			90.8(5)	
	$\langle M_{oct}\text{–}O\rangle$	*2.004*	$\langle M_{tet}\text{–}O\rangle$	*1.794*			178.1(8)	
0.3	*M*–O1	1.914(8) (2*x*)	*M*–O2	1.732(4) (*x*2)	0.116	141.6(1)	95.1(5)	172.0(3)
	M–O1	1.937(9) (2*x*)	*M*–O3	1.815(7)			87.3(7)	
	M–O2	2.171(3) (2*x*)	*M*–O3	1.875(6)			89.2(4)	
	$\langle M_{oct}\text{–}O\rangle$	*2.007*	$\langle M_{tet}\text{–}O\rangle$	*1.788*			177.5(8)	
0.5	*M*–O1	1.903(8) (2*x*)	*M*–O2	1.743(4) (*x*2)	0.131	141.3(1)	96.2(5)	172.4(3)
	M–O1	1.933(9) (2*x*)	*M*–O3	1.792(7)			87.3(7)	
	M–O2	2.194(3) (2*x*)	*M*–O3	1.862(6)			89.6(4)	
	$\langle M_{oct}\text{–}O\rangle$	*2.010*	$\langle M_{tet}\text{–}O\rangle$	*1.785*			176.5(8)	
0.7	*M*–O1	1.919(8) (2*x*)	*M*–O2	1.751(3) (*x*2)	0.143	140.5(1)	94.0(5)	170.5(2)
	M–O1	1.906(8) (2*x*)	*M*–O3	1.777(6)			87.2(6)	
	M–O2	2.215(3) (2*x*)	*M*–O3	1.840(6)			91.6(5)	
	$\langle M_{oct}\text{–}O\rangle$	*2.013*	$\langle M_{tet}\text{–}O\rangle$	*1.780*			178.8(7)	
1	*M*–O1	1.908(8) (2*x*)	*M*–O2	1.754(4) (*x*2)	0.163	140.8(1)	94.6(6)	170.4(2)
	M–O1	1.901(8) (2*x*)	*M*–O3	1.797(7)			87.0(6)	
	M–O2	2.250(3) (2*x*)	*M*–O3	1.813(7)			91.4(6)	
	$\langle M_{oct}\text{–}O\rangle$	*2.019*	$\langle M_{tet}\text{–}O\rangle$	*1.780*			178.4(8)	

[a] Included for comparison.

devoid of this property, such as in Ca_2FeAlO_5 [18]. Increasing the manganese content, a more pronounced elongation of the axial M_{oct}–O bonds and a systematic increase of the strain parameter (σ_{JT}) were observed (Table 3). Fig. 4 highlights the variation of the mean bond lengths along the *b*-axis ($\langle M\text{–}O2 \rangle$) and on the *a*,*c* plane ($\langle M\text{–}O1 \rangle$) with manganese content, illustrating the Jahn–Teller distortion enhancement due to the systematic increase of Mn^{3+} ions in the octahedral sites, in perfect accordance with the observed cell parameters variation.

Fig. 5 shows selected area ED patterns obtained for the $x = 0.2$, 0.5 and 1.0 compounds along the [$\bar{1}$01] zone axis. For the three compositions, all the reflections were indexed into a body-centered orthorhombic unit cell with parameters compatible with those calculated from the X-ray diffraction data.

The results from the Mohr's salt titration demonstrated that, contrary to Ca_2FeAlO_5, a small amount of M^{4+} ions were observed for the $x = 0.1$, 0.2 and 0.3 compounds. As no Fe^{4+} was detected by Mössbauer spectroscopy in these samples, it can be assumed that the determined amount of M^{4+} cations are exclusively due to Mn^{4+} ions. As expected, M^{4+} ions were not detected in the samples prepared under nitrogen.

3.1.2. Oxidized compounds

As previously referred, the as-prepared compounds with $x = 0.5$, 0.7 and 1.0 compositions were further annealed in air at 873 K in order to investigate their stability. After annealing, the XRD patterns showed that the brownmillerite structure for the $x = 0.5$ and 0.7 compounds was maintained, but significant changes were observed for the $x = 1.0$ sample. The determination of the structure by Rietveld refinement for the $x = 0.5$ and 0.7 compounds was carried out with the same model used for the as-prepared samples. Regarding the $x = 1.0$ composition, the best-fitted structure was achieved when a model similar to that of the $n = 3$ brownmillerite $Ca_2MnAlO_{5.5}$ [4] was used. However, the refinement was not fully completed, probably due to a mixture of the $n = 1$ and 3 phases. In fact, an oxygen pressure is necessary to produce the $Ca_2MnAlO_{5.5}$ compound, as previously reported [4]. In the present work, the samples were just annealed in air and the results clearly indicate that it is possible to perform oxygen insertion in the $Ca_2Fe_{1-x}Mn_xAlO_5$ compounds by this simple way, in agreement with the method used to oxidize $SrMn_{1-x}Ga_xO_{3-\delta}$ perovskite phases [19].

Table 4 summarizes the results of the Rietveld refinements as well as the M^{4+} content per formula unit determined by iodometric titration for the $x = 0.5$ and 0.7 samples annealed in air. Comparing the M^{4+} content obtained by titration with the results of the Mössbauer spectra, it can be deduced that both Fe^{4+} and Mn^{4+} are present, meaning that the thermal treatment at 873 K under air oxidized both Fe^{3+} and Mn^{3+} cations. Furthermore, as the Fe^{4+} amount per formula unit (0.02 for both $x = 0.7$ and 0.5) is much smaller than the calculated M^{4+} content for both samples ($M^{4+} = 0.07$ for $x = 0.5$ and $M^{4+} = 0.08$ for $x = 0.7$), it is possible to conclude about the preferred oxidation of Mn^{3+} relatively to Fe^{3+}.

The selected bond lengths and bond angles are shown in Table 5. From these results, a decrease of the orthorhombic distortion is observed, which is due to an increase of the *c* parameter together with a decrease of *a* and *b*, when comparing the annealed samples with those as-prepared. The comparison between bond lengths of the as-prepared and air annealed compounds (Tables 3 and 5, respectively) proves that the most significant differences were observed on the octahedral sites, where a decrease on the axial *M*–O2 bonds after air annealing was caused by a decrease of the Jahn–Teller effect, as corroborated by the σ_{JT} factor values. This fact is essentially related to the major role of the oxidation of some Mn^{3+} to Mn^{4+} ions. The performed oxidation treatments led to a consequent oxygen insertion, resulting in an oxygen over-stoichiometry (δ) between 0.03 and 0.04, in accordance to previous works on $Ca_2MnGaO_{5+\delta}$ compounds ($\delta = 0.045$, 0.09 and 0.39) [3,18].

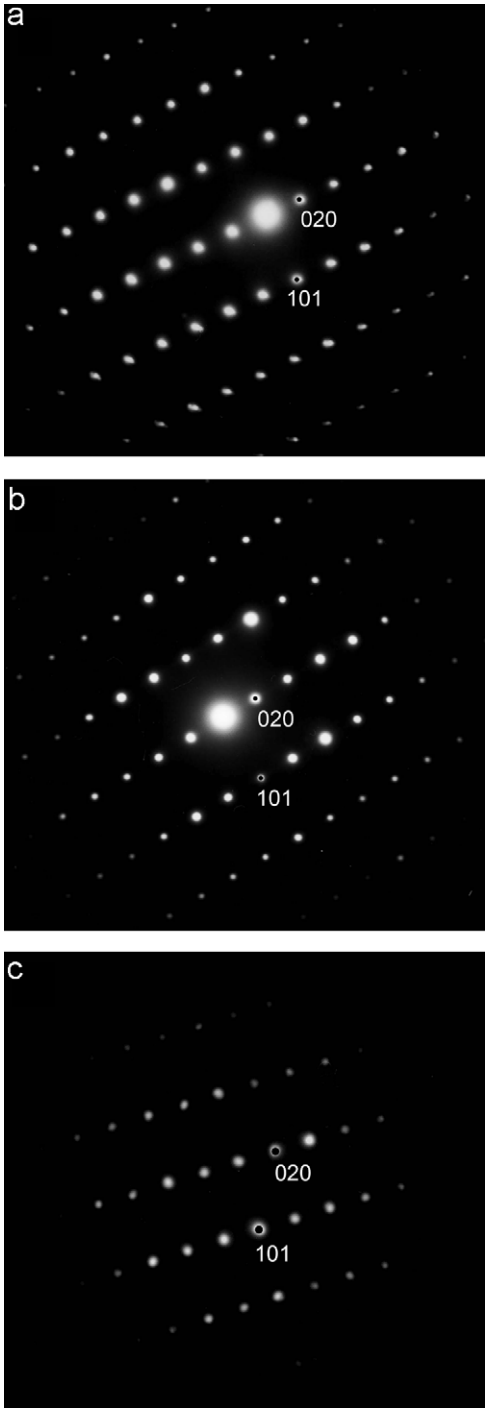

Fig. 5. [$\bar{1}$01] Electron diffraction patterns of the as-prepared compounds $Ca_2Fe_{1-x}Mn_xAlO_5$ for (a) $x = 0.2$, (b) $x = 0.5$ and (c) $x = 1.0$.

3.2. Mössbauer spectroscopy

The Mössbauer spectra obtained at 297 K (except for $x = 0$) and at 4 K are shown in Figs. 6 and 7. Those collected for Ca_2FeAlO_5 are

similar to reported data [11,13,20,21]. The spectra at 297 K indicate that $x \geqslant 0.1$ samples are paramagnetic at room temperature in contrast to Ca_2FeAlO_5 which is already magnetically ordered at this temperature. The spectra of non-oxidized samples were therefore fitted with two quadrupole doublets. The refined isomer shift, IS, and quadrupole splitting, QS, values, summarized in Table 6, are consistent with Fe^{3+} in tetrahedral and octahedral coordination. A third doublet with lower IS, consistent with Fe^{4+} [21] improved the fittings in the case of $x = 0.5$ and 0.7 oxidized samples. At 4 K all the samples are magnetically ordered. The widths of the observed peaks gradually increase with x within the range $0 < x < 0.5$ and become significantly broad for $x = 0.5$ and 0.7, due to the increasing number of different Fe nearest-neighbour configurations as Mn replaces Fe. This effect may be analysed considering distributions of magnetic hyperfine fields. However, in the case of $x = 0.5$ and 0.7 the magnetic ordering temperature, T_{ord}, is close to 4 K (see below, magnetization measurements section). As in the case of Ca_2FeAlO_5 at room temperature [21] or other oxides with chemical disorder close to the corresponding T_{ord} [22], spin fluctuations become important and broadening should be mainly attributed to relaxational effects rather than distribution effects.

Results obtained with the distributions model are therefore reliable for $0.1 \leqslant x \leqslant 0.3$ but should be taken with caution for $x = 0.5$ and 0.7 compounds. The average isomer shift, $\langle IS \rangle$ and magnetic hyperfine fields, $\langle B_{hf} \rangle$, are within the range of typical values for tetrahedrally and octahedrally coordinated Fe^{3+} and, in the case of the oxidized samples, also of Fe^{4+} [11,20,21]. Estimated relative areas are consistent with those deduced from the 297 K data.

The signs of quadrupole shifts, ε, for $x = 0.5$ and 0.7 samples are reversed relative to those of $0 \leqslant x \leqslant 0.3$ samples. As referred above, results for $x = 0.5$ and 0.7 should be taken with caution. However, for $0 \leqslant x \leqslant 0.3$ the absolute values of ε estimated for tetrahedral and octahedral Fe^{3+} steadily decrease. If these trends persist for $x > 0.3$ the sign reversal of ε values should take place for $x = 0.5$ and 0.7. Although the actual values of the estimated parameters for these samples may seem unreliable, a positive ε for the octahedrally coordinated Fe^{3+} sextets (with higher $\langle IS \rangle$ and $\langle B_{hf} \rangle$) and a negative ε for the tetrahedrally coordinated Fe^{3+} sextets (with lower $\langle IS \rangle$ and $\langle B_{hf} \rangle$) are very likely, since a sign reversal of these ε would have a dramatic influence on the shape of the spectra.

This reversal of the ε signs may be understood on the basis of different magnetic moments orientation of Fe and Mn in the browmillerite structure. Defining the orthorhombic axes in such a way that $c < a < b$, the internal magnetic field in $Ca_2Fe_2O_5$ and Ca_2FeAlO_5 is perpendicular to the b-axis [13] while in Ca_2MnAlO_5 it is parallel to this axis [12]. Assuming that the direction of the principal axes of the electric field gradient, at both tetrahedral and octahedral sites in $Ca_2Fe_{1-x}Mn_xAlO_{5+\delta}$ remain unchanged as in $Ca_2Fe_{2-y}Al_yO_5$ ($y = 0$, 1) [13], the ε values are expected to vary with x as shown in Table 6, if the direction of the magnetic moments gradually rotate from a direction perpendicular to b towards a direction parallel to this axis. Frustration caused by the

Table 4
Structural data and conventional Rietveld factors from the XRD data (S.G—*Ibm*2) of the oxidized compounds

	873 K; air	
	$x = 0.5$	$x = 0.7$
a (Å)	5.5054(2)	5.4891(2)
b (Å)	14.7286(5)	14.8111(5)
c (Å)	5.2989(2)	5.2796(2)
V (Å^3)	429.67(3)	429.23(3)
Atomic positions		
Ca (8*c*)		
x, y, z	0.0246(2); 0.11089(7); 0.4951(6)	0.0244(3); 0.11142(8); 0.4911(8)
Occup	1	1
B (Å^2)	0.71(3)	0.74(3)
M (4*a*)		
x, y, z	0; 0; 0	0; 0; 0
Occup	0.14(Fe); 0.11(Al); 0.25(Mn)	0.09(Fe); 0.06(Al); 0.35(Mn)
B (Å^2)	0.34(3)	0.44(4)
M (4*b*)		
x, y, z	0.9333(4); 0.25; 0.9575(6)	0.9314(5); 0.25; 0.9565(7)
Occup	0.11(Fe); 0.39(Al)	0.06(Fe); 0.44(Al)
B (Å^2)	1.01(6)	0.62(7)
O1 (8*c*)		
x, y, z	0.2549(8); 0.9890(2); 0.245(2)	0.256(1); 0.9890(2); 0.251(2)
Occup	1	1
B (Å^2)	1.11(6)	0.86(7)
O2 (8*c*)		
x, y, z	0.0639(5); 0.1447(2); 0.026(1)	0.0648(6); 0.1452(2); 0.035(1)
Occup	1	1
B (Å^2)	1.11(6)	0.86(7)
O3 (4*b*)		
x, y, z	0.865(1); 0.25; 0.626(1)	0.861(1); 0.25; 0.633(1)
Occup	0.5	0.5
B (Å^2)	1.6(2)	1.9(2)
Conventional Rietveld factors		
CR_{wp}	10.3	13.3
CR_p	8.26	10.7
R_{Bragg}	2.61	4.36
Iodometric titration		
M^{4+} (f.u.)	0.07	0.08

M^{4+} values per unit formula correspond to the iodometric titration results.

Table 5
Selected bond lengths (Å) and bond angles (deg) for the oxidized compounds

	M_{oct}–O		M_{tet}–O		σ_{JT}	M_{tet}–O2–M_{oct}	O1–M_{oct}–O1	O2–M_{oct}–O2
$x = 0.5$	*M*–O1	1.937(8) (2*x*)	M–O2	1.743(3) (2*x*)			93.3(4)	
873 K	*M*–O1	1.896(8) (2*x*)	M–O3	1.783(8)	0.125	141.8(1)	87.5(7)	172.7(2)
air	*M*–O2	2.179(3) (2*x*)	M–O3	1.889(6)			91.8(4)	
	$\langle M_{oct}–O \rangle$	*2.004*	$\langle M_{tet}–O \rangle$	*1.7895*			179.2(8)	
$x = 0.7$	*M*–O1	1.938(4) (2*x*)	M–O2	1.765(4) (2*x*)			93.6(5)	
873 K	*M*–O1	1.884(8) (2*x*)	M–O3	1.750(8)	0.132	140.9(2)	87.4(7)	170.2(3)
air	*M*–O2	2.188(4) (2*x*)	M–O3	1.856(8)			91.7(4)	
	$\langle M_{oct}–O \rangle$	*2.003*	$\langle M_{tet}–O \rangle$	*1.784*			178.9(8)	

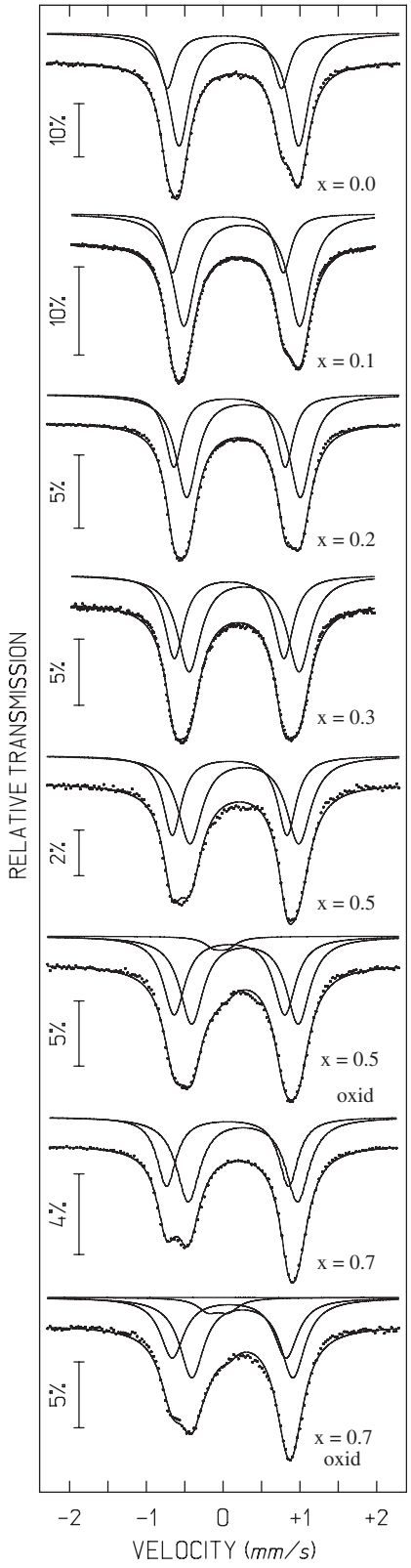

Fig. 6. Mössbauer spectra of the $Ca_2Fe_{1-x}Mn_xAlO_5$ compounds collected at 297 K, except for the $x = 0.0$ spectrum, measured at 363 K.

different magnetic moments orientation of Fe and Mn may also explain the strong decrease of T_{ord} with increasing x in the $Ca_2Fe_{1-x}Mn_xAlO_{5+\delta}$ series ($0 \leqslant x \leqslant 0.5$). For Ca_2MnAlO_5, where no competing interactions are present, T_{ord} is higher than for $Ca_2Fe_{1-x}Mn_xAlO_{5+\delta}$ for $x = 0.5$ and 0.7.

3.3. Magnetization measurements

The ZFC and FC magnetization curves collected at 0.05 T for all the as-prepared compounds are shown in Figs. 8 and 9, where the insets correspond to the inverse susceptibility plots. All the $M(T)$ curves display some degree of irreversibility below a certain temperature, although different behaviours are detected for samples with $x \leqslant 0.3$ and $x \geqslant 0.5$. The $M(T)$ curves for the samples with $x = 0$, 0.1 and 0.2 present a small kink at 340, 250 and 160 K, respectively, easily detected in the inverse susceptibility plots. In agreement with the Mössbauer results, these temperatures were considered to define the transition temperature from the paramagnetic to the magnetic state.

Magnetization as a function of the applied magnetic field, $M(H)$, has been measured for all samples and the $M(H)$ curves evidence an overall antiferromagnetic behaviour for all of them. This can be seen in Fig. 10 where the results obtained for some of the compounds are shown. In this figure, the linear fits to the first 10 points (fields up to 0.1 T) obtained at the higher temperatures, allow to verify that, for samples with $x < 0.3$, those fits only reproduce all the experimental $M(H)$ measurements for temperatures above the kink temperature value, where the compounds are paramagnetic. Based on the behaviour of $M(H)$ curves, the ordering temperature of the $x = 0.3$ compound can be estimated around 100 K, the correspondent kink being hidden in the $M(T)$ curve by the magnetization increase below 150 K.

As in the case of Ca_2FeAlO_5, where the transition around 340 K has been attributed to the onset of an antiferromagnetic order between the Fe^{3+} ions laying in the octahedral planes [11], the magnetic transitions corresponding to the kinks observed on the $M(T)$ curves of our compounds are attributed to the antiferromagnetic ordering of the Fe ions also occupying the octahedral sites. As confirmed by the decrease of the ordering temperature for samples with x from 0 to 0.3, the strength of the long-range antiferromagnetic order is strongly reduced when Fe ions are substituted by Mn ions.

For samples with $0.1 \leqslant x \leqslant 0.3$, the difference between ZFC and FC measurements at low temperatures as well as the total magnetic moment are enhanced as Mn content increases (Fig. 8). In the three cases the ZFC curves present a maximum at 5, 8 and 20 K, and decrease at low temperatures, while the FC curves increase for $x = 0.2$ and 0.3. In this type of compounds, such behaviour is generally associated with the existence of magnetic frustration. As previously discussed, certain degree of structural and chemical disorder exists, even in Ca_2FeAlO_5, since octahedral and tetrahedral sites are occupied by both Fe and Al ions, which have different ionic radii. Also a significant structural distortion is induced by the substitution of Fe^{3+} by Mn^{3+}, due to the Jahn–Teller character of this ion (see Fig. 4 and Table 3). In addition, the fact that in Ca_2FeAlO_5 the Fe magnetic moments are aligned perpendicularly to the b-axis [13], while in Ca_2MnAlO_5 [12] and Ca_2FeMnO_5 [23] the Fe moments are aligned along the b-axis, suggests that magnetic frustration has to be present in the case of our compounds $Ca_2(Fe,Mn)AlO_5$, where all metal ions (Fe, Mn and Al) occupy octahedral sites.

In the case of the $x \geqslant 0.5$ samples, from the $M(T)$ curves (Fig. 9), it can be concluded that Fe substitution by Mn increases the ordering temperature since the temperature values where the ZFC and FC curves come apart increase from around 35 and 45 K for the $x = 0.5$ and 0.7 samples, respectively, to 150 K for

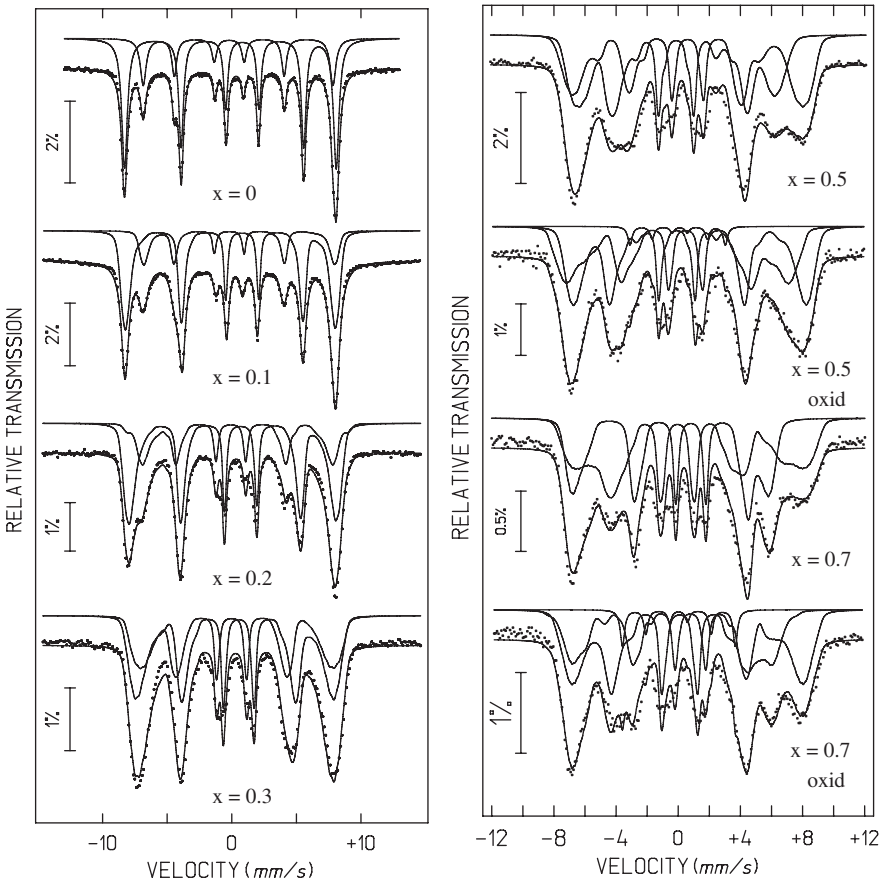

Fig. 7. Mössbauer spectra of the $Ca_2Fe_{1-x}Mn_xAlO_5$ compounds collected at 4 K.

Ca_2MnAlO_5 ($x = 1$). As in these samples the Mn ions occupy 50%, 70% and 100% of the octahedral sites, the increase of the ordering temperature values is explained by the fact that the Mn^{3+}–Mn^{3+} coupling prevails and is responsible for the long-range antiferromagnetic order occurring within the octahedral layer, being reinforced as Mn content increases.

The magnetization in both ZFC and FC curves of the $x = 0.5$ and 0.7 samples increases with decreasing temperature after the splitting of the curves, in contrast to the $x \leqslant 0.3$ compounds (Figs. 9 and 8). In order to better evaluate the low-temperature behaviour of the two groups of samples ($x \leqslant 0.3$ and $x \geqslant 0.5$) IRM and TRM measurements were performed at 5 K for the $x = 0.3$ and 0.7 samples. As can be seen in Fig. 11, for the $x = 0.3$ sample the IRM curve approaches saturation above 3 T, almost reaching the TRM curve. In contrast, in the $x = 0.7$ compound, the IRM curve increases continuously up to the maximum measured field (5.5 T), the correspondent magnetization value being still far from the TRM curve. Besides the distinction between the compounds due to the different character of the prevailing interactions (Fe^{3+}–Fe^{3+} for $x = 0.3$ and Mn^{3+}–Mn^{3+} for $x = 0.7$) the low-temperature response of the $Ca_2Fe_{0.7}Mn_{0.3}AlO_5$ compound is reminiscent of a spin-glass behaviour. This can be explained on the basis of the magnetic frustration due to the chemical disorder resulting from the occupation of the octahedral layers by different metals, more important in the samples with lower manganese content, in addition to the competition between different magnetic moments orientations. Due to the increasing Jahn–Teller effect, the magnetic anisotropy has an increasing role in the $x \geqslant 0.5$ compounds. For the $x = 1$ sample, the magnetic behaviour revealed in the $M(T)$ curves at low temperature was previously attributed to the canting of the Mn moments [12]. Therefore, a small canted antiferromagnetic alignment between the Mn moments is also expected in the case of the $x = 0.7$ compound.

Rykov and co-workers [23] investigated the Ca_2FeMnO_5 compound and their results are consistent with the model of an Ising ferrimagnet. In the case of our compounds $Ca_2Fe_{1-x}Mn_xAlO_5$ the presence of the non-magnetic aluminium ions, essentially located in the tetrahedral sites, breaks the coupling between octahedral layers, along the *b*-axis. This supports the interpretation that the magnetic properties of the $Ca_2Fe_{1-x}Mn_xAlO_5$ compounds are determined by the coupling between the magnetic moments occupying octahedral sites (*a*–*c* plane), dominated by Fe^{3+}–Fe^{3+} interactions in the case of $x \leqslant 0.3$ samples and by Mn^{3+}–Mn^{3+} interactions for the $x \geqslant 0.5$ compositions.

Table 7 presents the effective magnetic moment values extracted from the analysis of the inverse susceptibility plots (Fig. 8) for both as-prepared and oxidized samples. In all cases, the obtained values are smaller than the spin-only values considering the relative quantities of high-spin $3d^5$ Fe^{3+} and $3d^4$ Mn^{3+} ions (decreasing from 5.8 μ_B for $x = 0.1$ until 5.2 μ_B for $x = 0.7$). This difference may be understood by local correlations between the magnetic moments, still existing in the temperature range used to the Curie–Weiss analysis. The negative values obtained for the paramagnetic Curie temperatures confirm the antiferromagnetic

Table 6
Estimated parameters from the Mössbauer spectra of $Ca_2Fe_{1-x}Mn_xAlO_{5+\delta}$ taken at different temperatures

x	T/K	IS, $\langle IS \rangle$ (mm/s)	QS, ε (mm/s)	B_{hf}, $\langle B_{hf} \rangle$ (T)	Γ (mm/s)	I (%)	Fe (f.u.)
0	363	0.30	1.61		0.26	76.7	0.77 oct
		0.09	1.54		0.26	23.3	0.23 tet
	4	0.48	−0.92	50.4	0.26	74.8	0.75 oct
		0.28	0.69	45.2	0.26	25.2	0.25 tet
0.1	297	0.36	1.59		0.37	73	0.66 oct
		0.17	1.52		0.26	27	0.24 tet
	4	0.46	−0.92	49.9	*	75	0.68 oct
		0.30	0.78	45.1		25	0.22 tet
0.2	297	0.38	1.54		0.36	65	0.52 oct
		0.19	1.51		0.28	35	0.28 tet
	4	0.48	−0.63	48.7	*	68	0.54 oct
		0.30	0.52	45.2		32	0.26 tet
0.3	297	0.39	1.51		0.38	54	0.38 oct
		0.19	1.50		0.33	46	0.32 tet
	4	0.50	−0.30	45.6	*	58	0.41 oct
		0.30	0.40	45.0		42	0.29 tet
0.5	297	0.38	1.48		0.39	59	0.30 oct
		0.18	1.56		0.30	41	0.20 tet
	4#	0.44	0.92	41.4	*	57	0.29 oct
		0.28	−0.88	38.6		43	0.21 tet
0.7	297	0.37	1.42		0.37	60	0.18 oct
		0.17	1.59		0.30	40	0.12 tet
	4#	0.45	0.78	41.3	*	57	0.17 oct
		0.27	−1.30	37.8		43	0.13 tet
0.5 oxid	297	0.39	1.45		0.37	53	0.27 oct
		0.19	1.50		0.36	43	0.21 tet
	4#	0.05	0.18		0.31	4	0.02 Fe^{4+}
		0.44	0.83	43.5		50	0.25 oct
		0.31	−0.53	41.5	*	47	0.23 tet
		0.14	−0.13	19.0		3	0.02 Fe^{4+}
0.7 oxid	297	0.36	1.37		0.39	54	0.16 oct
		0.18	1.55		0.39	39	0.12 tet
		0.03	0.47		0.34	7	0.02 Fe^{4+}
	4#	0.46	0.51	43.0	*	56	0.17 oct
		0.31	−1.17	38.0		38	0.11 tet
		0.14	0.02	22.5		6	0.02 Fe^{4+}

IS isomer shift relative to metallic α-Fe at 295 K; QS quadrupole splitting; $\varepsilon = (e^2V_{ZZ}Q/4)(3\cos^2\theta - 1)$ quadrupole shift. Γ line-widths; *$\Gamma = 0.26$ mm/s for lorentzian peaks in distributions of magnetic hyperfine fields; $\langle IS \rangle$, $\langle B_{hf} \rangle$ average IS and magnetic hyperfine fields estimated for these distributions. I relative areas. Except for spectra # (see text), estimated errors are <0.02 mm/s for IS, QS, ε, <0.4 T for $\langle B_{hf} \rangle$ and $<2\%$ for I.

character of all compounds. In the case of the oxidized samples, for which the $M(T)$ and $M(H)$ measurements reveal magnetic behaviours very similar to the as-prepared samples with the same composition, the lower value of the effective moment (Table 7) is in agreement with the oxidation of some Fe^{3+} and Mn^{3+} ions, as detected by Mohr salt titrations and Mössbauer spectroscopy.

4. Conclusions

The compounds $Ca_2Fe_{1-x}Mn_xAlO_{5+\delta}$ ($0 \leqslant x \leqslant 1.0$) were successfully synthesized under air ($x \leqslant 0.3$) or nitrogen ($x \geqslant 0.5$). XRD and ED patterns for the as-cast samples are consistent with the brownmillerite structure. With the increase of manganese content, a systematic decrease of both a and c cell parameters and an increase of b occurred, clearly indicating the influence of the Jahn–Teller effect of the Mn^{3+} ions, in accordance with the systematic increase of the M–O2 mean bond length.

The annealing under air of the samples previously prepared under nitrogen ($x = 0.5$ and 0.7) induced the oxidation of some M^{3+} ions (M = Fe, Mn), leading to a final composition $Ca_2Fe_{1-x}Mn_xAlO_{5+\delta}$ with δ between 0.03 and 0.04. Mössbauer spectra confirmed the presence of Fe^{4+} in these samples and the comparison with the chemical titrations results suggested a preferred oxidation of Mn^{3+} relative to Fe^{3+}.

The fact that oxidized compounds are easily obtained suggests that higher oxygen content compounds may be achieved using other synthesis conditions, leading ultimately to mixed valence manganese systems with magnetoresistance effects, as observed for $SrCaMnGaO_{5+\delta}$ [9].

The magnetic characterization showed that the ordering temperature decreases as Mn content increases in the case of the $x \leqslant 0.3$ samples where the long-range order is dominated by Fe^{3+}–Fe^{3+} interactions and increases with x for the $x \geqslant 0.5$ compounds, where Mn^{3+}–Mn^{3+} coupling prevails.

Data crossing between Mössbauer spectroscopy and magnetic measurements allows to conclude that the substitution of Fe by Mn in $Ca_2Fe_{1-x}Mn_xAlO_5$ weakens the Fe^{3+}–Fe^{3+} coupling interaction, inducing magnetic frustration and canted antiferromagnetism.

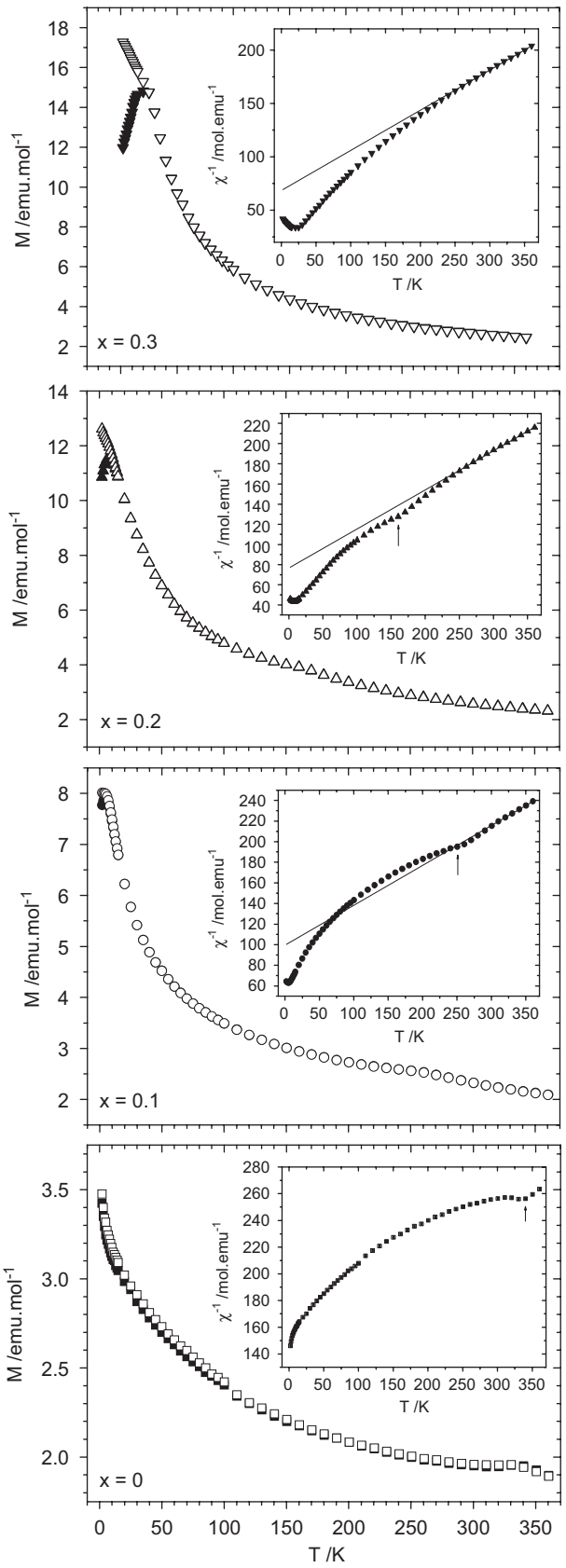

Fig. 8. $M(T)$ curves collected at 0.05 T for the as-prepared samples with $x \leqslant 0.3$: ZFC—solid symbols; FC—open symbols. The insets show the inverse susceptibility curves and the linear fits to the susceptibility values in the temperature range 320–360 K.

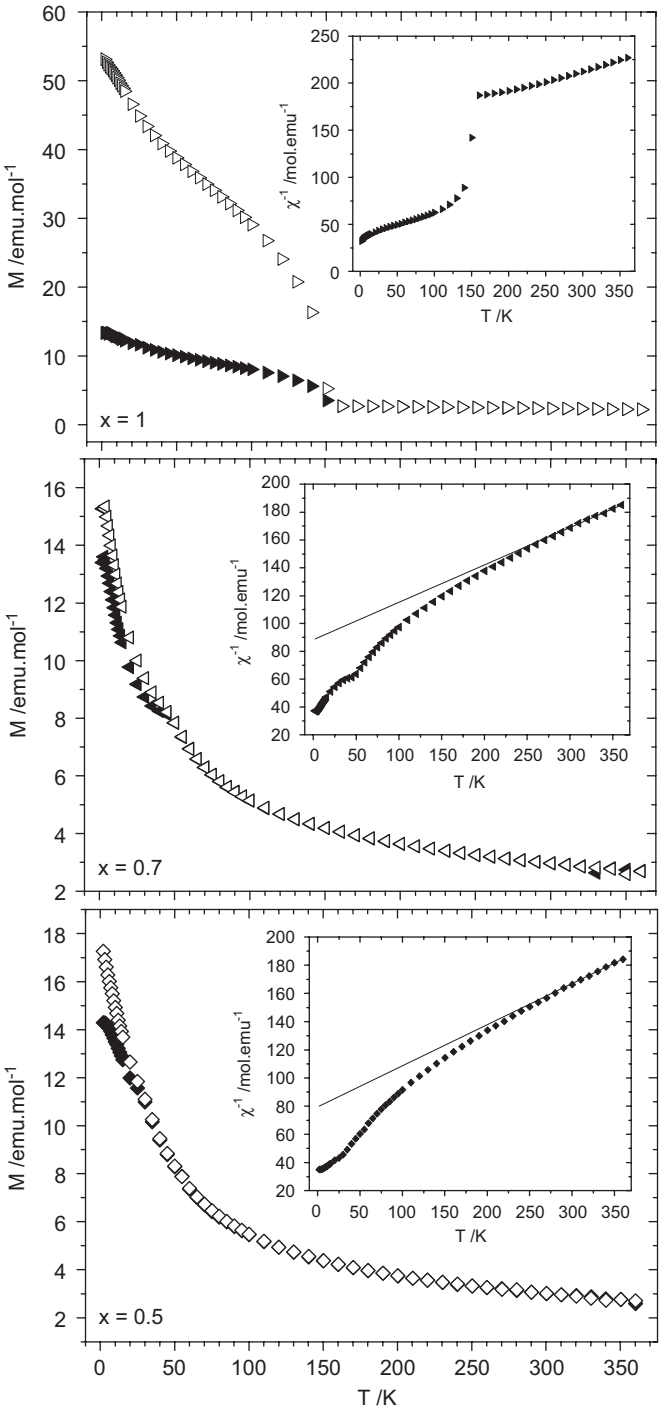

Fig. 9. $M(T)$ curves collected at 0.05 T for the as-prepared samples with $x \geqslant 0.5$: ZFC—solid symbols; FC—open symbols. The insets show the inverse susceptibility curves and the linear fits to the susceptibility values in the temperature range 320–360 K.

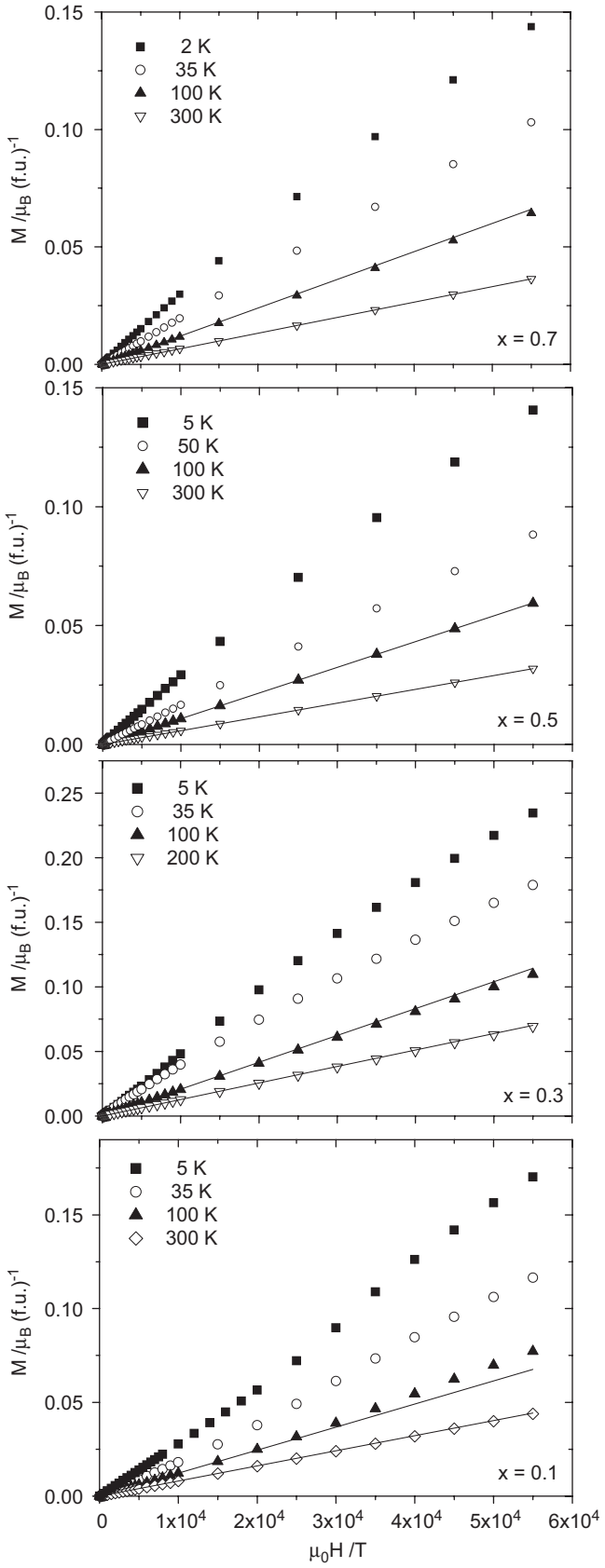

Fig. 10. Magnetization versus applied magnetic field collected at different temperatures. The straight lines are linear fits to the data points obtained for fields up to 0.1 T.

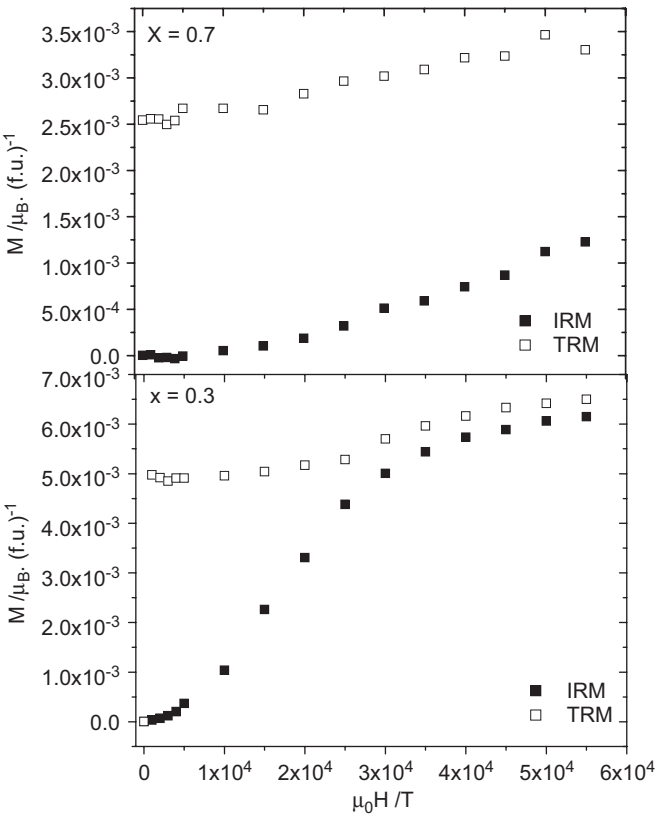

Fig. 11. Isothermal remanent magnetization (IRM) and thermoremanent magnetization (TRM) measured at 5 K.

Table 7
Mn content (x), effective magnetic moment (μ_{eff}) and paramagnetic Curie temperature (θ_p) for $Ca_2Fe_{1-x}Mn_xAlO_{5+\delta}$ compounds

x	μ_{eff} (μ_B)	θ_p
0.1	4.53(2)	−254(4)
0.2	4.57(2)	−212(4)
0.3	4.75(2)	−215(4)
0.5	4.97(2)	−205(4)
0.7	5.06(2)	−211(4)
0.5 (ox)	4.93(2)	−200(4)
0.7 (ox)	4.86(2)	−188(4)

Acknowledgements

This work was supported by FCT, POCI, and co-financed by FEDER (POCI/QUI/58915/2004). E. Tsipis acknowledges FCT, Portugal, for the post-doctoral Grant SFRH/BPD/28629/2006.

References

[1] F. Lindberg, G. Svensson, S.Ya. Istomin, S.V. Aleshinskaya, E.V. Antipov, J. Solid State Chem. 177 (2004) 1592–1597.
[2] P. Berastegui, S.G. Eriksson, S. Hull, Mater. Res. Bull. 34 (1999) 303–314.
[3] A.M. Abakumov, M.G. Rozova, B.Ph. Pavlyuk, M.V. Lobanov, E.V. Antipov, O.I. Lebedev, G. van Tendeloo, D.V. Sheptyakov, A.M. Balagurov, F. Bourée, J. Solid State Chem. 158 (2001) 100–111.
[4] H.M. Palmer, A. Snedden, A.J. Wright, C. Greaves, Chem. Mater. 18 (2006) 1130–1133.

[5] A.M. Abakumov, M.G. Rozova, A.M. Alekseeva, M.L. Kovba, E.V. Antipov, O.I. Lebedev, G.V. Tendeloo, Solid State Sci. 5 (2003) 871–882.
[6] P.D. Battle, S.J. Blundell, P.N. Santhosh, M.J. Rosseinsky, C. Steer, J. Phys.: Condens. Matter 14 (2002) 13569–13577.
[7] A.M. Abakumov, M.G. Rozova, B.Ph. Pavlyuk, M.V. Lobanov, E.V. Antipov, O.I. Lebedev, G.V. Tendeloo, O.L. Ignatchik, E.A. Ovtchenkov, Yu.A. Koksharov, A.N. Vasil'ev, J. Solid State Chem. 160 (2001) 353–361.
[8] A.J. Wright, H.M. Palmer, P.A. Anderson, C. Greaves, J. Mater. Chem. 11 (2001) 1324–1326.
[9] P. Battle, A.M.T. Bell, S.J. Blundell, A.I. Coldea, D.J. Gallon, F.L. Pratt, M.J. Rosseinsky, C.A. Steer, J. Solid State Chem. 167 (2002) 188–195.
[10] A.A. Colville, S. Geller, Acta Crystallogr. B 27 (1971) 2311–2315.
[11] J. Malveiro, T. Ramos, L.P. Ferreira, J.C. Waerenborgh, M.R. Nunes, M. Godinho, M.D. Carvalho, J. Solid State Chem. 180 (2007) 1863–1874.
[12] A.J. Wright, H.M. Palmer, P.A. Anderson, C. Greaves, J. Mater. Chem. 12 (2002) 978–982.
[13] R.W. Grant, J. Chem. Phys. 51 (1969) 1156–1162.
[14] M. Zotzl, H. Pollmann, J. Am. Ceram. Soc. 89 (2006) 3491–3497.
[15] T. Roisnel, J. Rodriguez-Carvajal, FullProf Suite, April 2005.
[16] J.C. Waerenborgh, M.O. Figueiredo, J.M.P. Cabral, L.C.J. Pereira, Phys. Chem. Miner. 21 (1994) 460–468.
[17] R.D. Shannon, Acta Crystallogr. A 32 (1976) 751–769.
[18] A.M. Abakumov, M.G. Rozova, E.V. Antipov, Russ. Chem. Rev. 73 (2004) 847–860.
[19] E.N. Caspi, M. Avdeev, S. Short, J.D. Jorgensen, B. Dabrowski, O. Chmaissem, J. Mais, S. Kolesnik, J. Solid State Chem. 177 (2004) 1456–1470.
[20] A.L. Shaula, Y.V. Pivak, J.C. Waerenborgh, P. Gaczyński, A.A. Yaremchenko, V.V. Kharton, Solid State Ionics 177 (2006) 2923–2930.
[21] J.C. Waerenborgh, D.P. Rojas, N.P. Vyshatko, A.L. Shaula, V.V. Kharton, I.P. Marozau, E.N. Naumovich, Mater. Lett. 57 (2003) 4388–4393.
[22] R.E. Vandenberghe, E. De Grave, Mössbauer effect studies of oxidic spinels, in: G.L. Long, F. Grandjean (Eds.), Mössbauer Spectroscopy Applied to Inorganic Chemistry, vol. 3, Plenum Press, New York, 1989.
[23] A.I. Rykov, K. Nomura, Y. Ueda, A.N. Vasiliev, J. Magn. Magn. Mater. 320 (2008) 950–956.